Development of a Heterogeneous Microstructurally Based Finite Element Model for the Prediction of Forming Limit Diagram for Sheet Material

XINJIAN DUAN, MUKESH JAIN, and DAVID S. WILKINSON

A heterogeneous finite element model with randomly distributed inhomogeneities has been developed for the determination of the forming limit diagram (FLD) for thin aluminum sheet material based on the prediction of localized necking. The strength difference between the inhomogeneities and the matrix is ascertained either from the fluctuation of the experimental stress-strain curve or from a micromechanical analysis that uses a representative particle field. By changing the specimen geometry and friction conditions, different stress states (or strain paths) are achieved. A plot of the critical Oyane fracture parameter is used to identify the limit strain state. Also, a plot of equivalent plastic strain rate is used to distinguish the boundary of intense shear bands and hence to identify where to take the measurement point. Both a plane stress model and a three-dimensional (3-D) model are adopted to predict the shear banding phenomenon and hence the FLD. The predicted FLD agrees well with the measurements from a recent round robin experimental FLD involving several independent research laboratories. The Taguchi method is applied to assess how the various parameters involved in the heterogeneous model affect the calculated forming limit strain.

I. INTRODUCTION

KNOWING the limits of formability is important for full utilization of any material's capabilities. The forming limit diagram (FLD) is perhaps the most accepted means of characterizing formability. The FLD defines the extent to which a sheet material can be deformed over a wide monotonic range of strain paths. This capability is limited by the occurrence of localized thinning in the form of an intense shear band, as shown in Figure 1 for both aluminum alloys and steel under uniaxial tension, and in Figure 2 under biaxial loading. However, the measurement of FLDs is tedious and time-consuming. Thus, many attempts have been made to predict FLDs.[1–6] One challenge lies in relating the way in which the FLD is determined experimentally to the methodology used in the numerical predictions. For example, the deterministic parameters used to get the predicted FLD lead to a single curve in major-minor strain space, while experimentally measured FLDs often show a large scatter.[7] Such a pronounced difference adds to the discrepancy between the experimental and numerical FLDs.

One of the major sources of the scatter in the determination of an FLD comes from the selection of measurement points near the fracture plane. There are two generally accepted rules: (1) the grids (square or circle) must still be intact and (2) the grids must be imminently adjacent to the fracture surface. A combination of these two rules implies that, in Figure 2, points A, B, and C are all valid measurement points while point D is invalid.

In sheet materials, an intense shear band is frequently observed ahead of fracture. Once the band forms, the strain value within the band increases dramatically. If a complete grid is partially located within the intense shear band (point E in Figure 2), the validity of the grid strains becomes somewhat questionable. The relative position of the FLD will then change depending on whether such grids are included. There is no generally accepted evaluation strategy.

From the experimental method, it is clear that the FLD is associated with the localized necking. Specifically, the forming limit corresponds to the *onset* of localized necking. It is often difficult to experimentally stop the test just at this point due to the test control and signal measurement limitations of formability test machines. Hence, highly necked or fractured specimens are generally used to obtain the forming limit strains. Numerical simulation is not subjected to the same restrictions, and a suitable localization criterion (Hill,[8] for example) can be applied to evaluate the occurrence of shear localization.

It is well known that the FLD is affected by a material's microstructure. With this in mind, we have recently developed a microstructurally based model that incorporates the influence of a spatially inhomogeneous distribution of local strengths on localized necking.[9] This has now been incorporated into a two-scale (micromacro) model in order to consider the effect of the distribution, size, and morphology of particles on the postnecking mechanical behavior of various Al-Mg alloys such as AA5182-O aluminum alloy. This alloy was chosen because it was used in a recent round robin experimental FLD program involving several research laboratories.[10] Both an in-plane plane stress model and a three-dimensional (3-D) model of the Nakajima test[11] are used. Four major local microstructural parameters (local strength difference and the volume fraction of soft and hard phases) involved in the heterogeneous models are studied by the Taguchi method[12] to determine their individual contribution to the calculated forming limit strain.

XINJIAN DUAN, Senior Stress Analyst, is with the Atomic Energy of Canada Limited, Mississauga, ON Canada. MUKESH JAIN, Associate Professor, Department of Mechanical Engineering, and DAVID S. WILKINSON, Professor, Department of Materials Science and Engineering, Director, McMaster Manufacturing Research Institute, and Director, McMaster Centre for Automotive Materials, are with McMaster University, Hamilton, ON, Canada L8S 4L7.

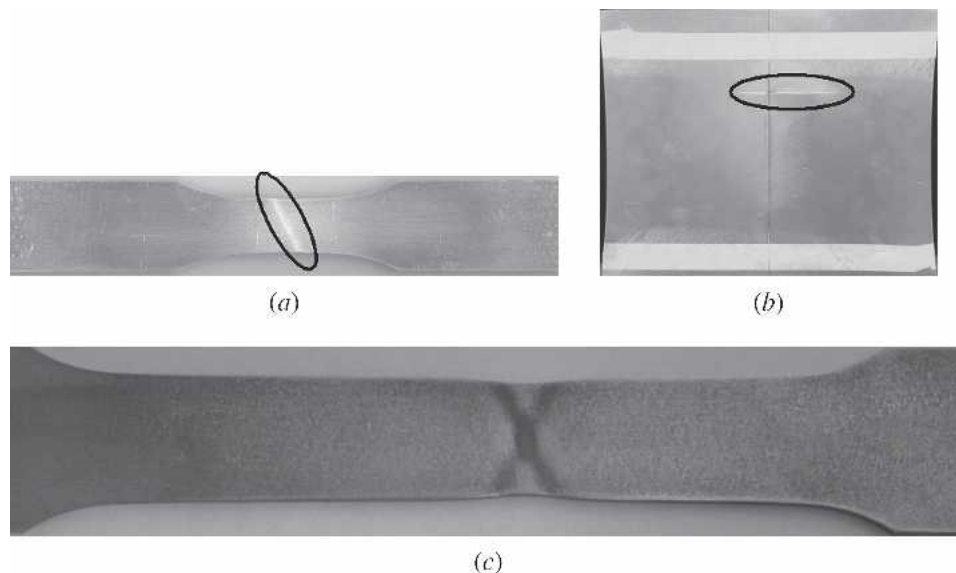Manuscript submitted July 5, 2005.

Fig. 1—Experimental observed intense shear bands under (*a*) plane stress deformation mode and (*b*) plane strain deformation mode for Al alloys. (*c*) Crossed shear bands in dual-phase steel DP600.
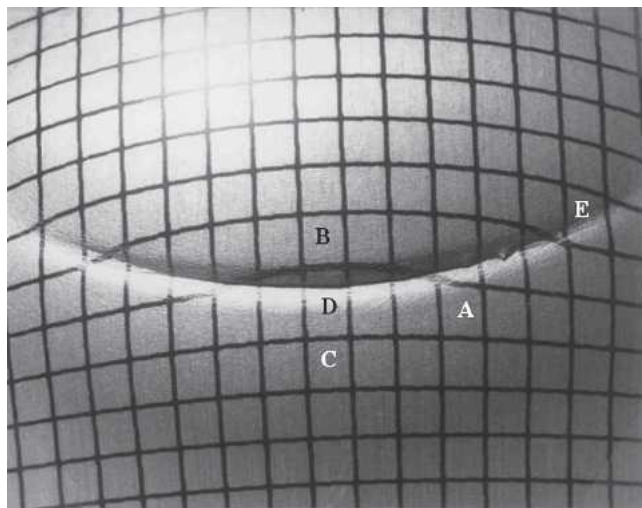

Fig. 2—Illustration of selecting valid measurement points for a specimen deformed by hemispherical punch.

II. FINITE ELEMENT MODELS

Summarizing the work on the numerical prediction of FLDs in the literature, two kinds of finite element models can be categorized: an in-plane plane stress model and a 3-D model with complex contact and friction. Because we are interested in thin sheet material, an in-plane plane stress model is commonly used, which ignores the thickness stress distribution. Although it is experimentally difficult to apply perfect in-plane biaxial loading, it is easy to do so in the numerical simulation. As the contact and friction algorithm are not involved in this type of in-plane plane stress model, the required computing resource is minimum. However, if the predicted FLD is compared with the measurements obtained by the most commonly used Nakajima test, which uses a hemispherical punch, no matter how

accurate the predicted FLD is, one will still question the feasibility of such a comparison because contact stress and friction are unavoidable in the real test. Hence, it would be of interest to compare the predicted FLDs from these two models.

A number of heterogeneous finite element models have been developed to treat the effect of local microstructure (*i.e.,* texture, grain size, particle distributions, *etc*.) on the forming limit strains. For the in-plane plane stress model, the different strain paths can be determined by changing either the specimen geometry such as the notch radius R (defined in Figure 3) or by changing the loading ratio $r = a_2/a_1$, as shown in Figure 4 where a_1 and a_2 are the applied displacements in two orthogonal directions of the sheet. A typical setup for a Nakajima test is shown in Figure 5. By changing the width of the blank (Figures 6(a) through (d)), different strain paths on the left side on the FLD could be obtained. To acquire the limit strain of the right side of FLD, different friction conditions are applied to the full circular blank (Figure 6(e)). For reasons of clarity, the spatial distribution of inhomogeneities is not presented in Figure 6.

In the simulations presented in this work, the von Mises yield criterion is used. The general purpose FE package MSC.Marc is used as the analysis tool. Based on prior analyses,[13] four-node full integration elements with assumed strain formulation are adopted for the in-plane plane stress model. The shell element with reduced integration is used for the 3-D simulation.

III. INHOMOGENEITIES

Most commercially produced alloys have inhomogeneities present at different length scales. At the mesoscale, texture is a major source. In AA5182, for example, the cube-oriented grains are weaker while the Goss-oriented grains are stronger. The volume fraction of each component

in an alloy has been easily measured using X-ray diffraction or electron backscattered diffraction (EBSD). The strength difference between the regions with average behavior that we call the "matrix" and the inhomogeneities can also be quantitatively calculated by the use of the Fourier transformation from measured EBSD data.[14] In this work, we simplify the analysis and treat inhomogeneity phenomenologically by assigning regions that have a slightly higher or lower strength than the matrix. The matrix, which forms the majority of the material, is assumed to have the average stress-strain response (Figure 7). The stress-strain curves for the "hard" and "soft" components are simply obtained by slightly shifting the stress-strain curve for the matrix up or down ±2 pct. Thus, the work-hardening rate for all three phases is maintained the same. All stress-strain curves are fitted into the Voce equation.[15] The stress-strain curves determined from Figure 7 are termed phenomenological stress-strain curves. One can see that the strength differences fall within the range of experimental error. The stress-strain curves determined from the two-scale (micromacro) modeling in the following are termed as microstructurally based stress-strain curves, as discussed in Section IV. Their influence on the predicted FLD will be discussed later.
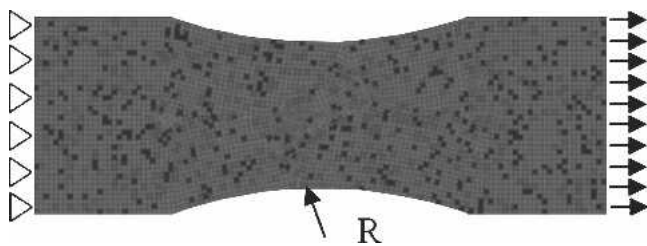

Fig. 3—Finite element model used to determine the left side of the FLD.

IV. TWO-SCALE MODELING

At the microlength scale, the second-phase particles are a major source of inhomogeneity. Figure 8 shows a particle field of an Al-Mg alloy. Using a micromechanical analysis, the influence of such local microstructure can be incorporated in the structural model. In other words, the stress-strain curves associated with inhomogeneities can be obtained from the micromechanical analyses using a series of unit cell models.

To simulate how local particle size, morphology, and distribution affect the macroscale response, a micromacro two-scale modeling strategy is used. In brief, the procedure is introduced as follows. (1) Measurement of individual particle position and size using image analysis software. (2) Construction of a virtual particle field using suitable preprocessing finite element software. (3) Micromechanical analyses based on the representative volume elements or concentric windows of varying size. (4) The stress-strain curves from the micromechanical analyses are assigned randomly to different elements in the structural model. (5) Elements close to the predicted intense shear bands in the structural model are selected to extract forming limit strains.

Figure 9(a) shows the constructed virtual particle field and three concentric windows for the micromechanical analysis. Each particle is assumed to be an ellipse. The corresponding finite element model for the medium size window is shown in Figure 9(b). There are two phases in each window: the white particles and the remaining matrix. All particles are assumed to only undertake elastic deformation, with a Young's modulus of 300 GPa and Poisson's ratio of 0.28. The flow stress of the matrix is assumed to follow the average response from the uniaxial tension test. In other words, the curve identified as "Voce equation fitting_Matrix" is assigned to be the matrix material in Figure
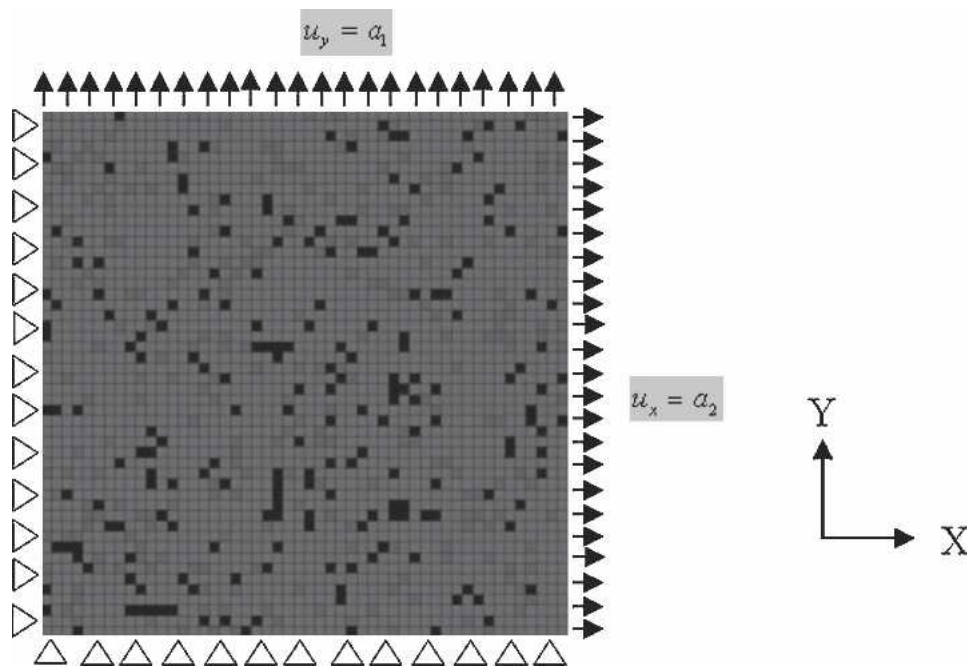

Fig. 4—Finite element model used to determine the right side of the FLD, in which a_1 and a_2 are the applied loads.
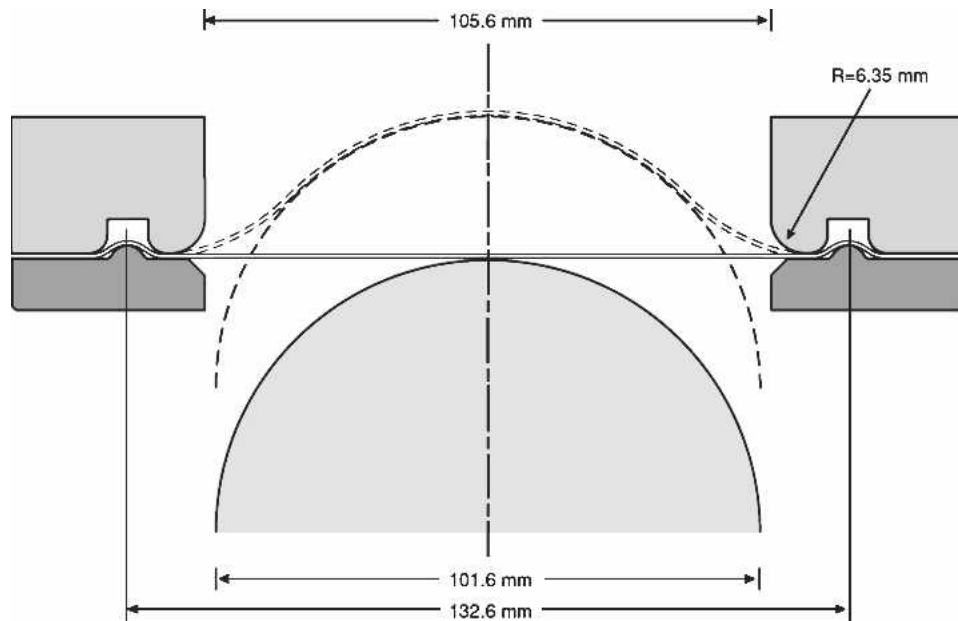
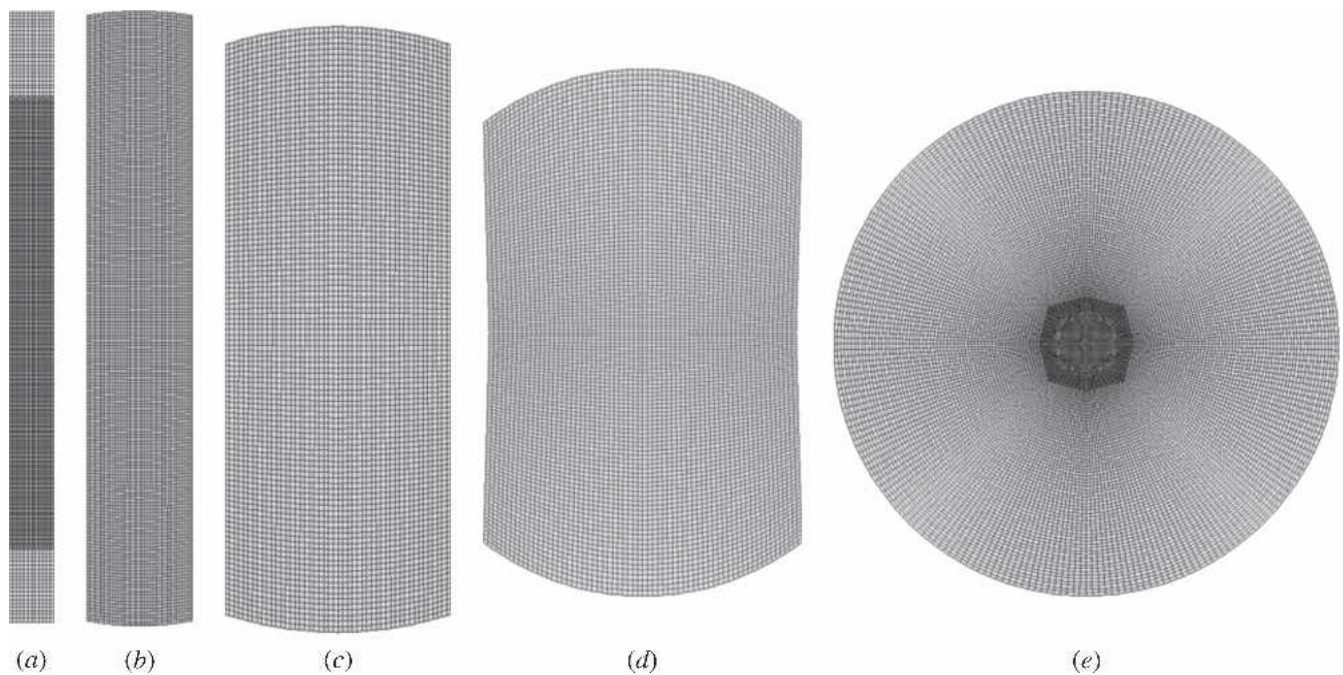Fig. 5—A schematic of the tool setup for the Nakajima test.

Fig. 6—Blanks used to determine the FLD in the Nakajima test.

9(b). This is an approximation because it is known that the matrix material at the microscale in Figure 9(b) changes from place to place. However, this is a common practice in such micromechanical analysis.

The boundary conditions of Figure 9(b) are such that the top and bottom edges are maintained straight during deformation, the left edge is constrained, and a uniform displacement is applied to the right edge. The calculated responses from the three selected windows are presented in Figure 10.

The initial part of the stress-strain curve is identical for all these windows. However, because the particle characteristics (such as the particle cluster and the volume fraction of particles) vary from window to window, one would expect to see different behavior at high strain (*i.e.*, shear localization). This is seen by the strain at which the stress drop occurs: the window that fails earlier, the soft phase; and that which fails later, the hard phase. The remaining one is referred to as the matrix. The effect of window or unit cell

3492—VOLUME 37A, DECEMBER 2006

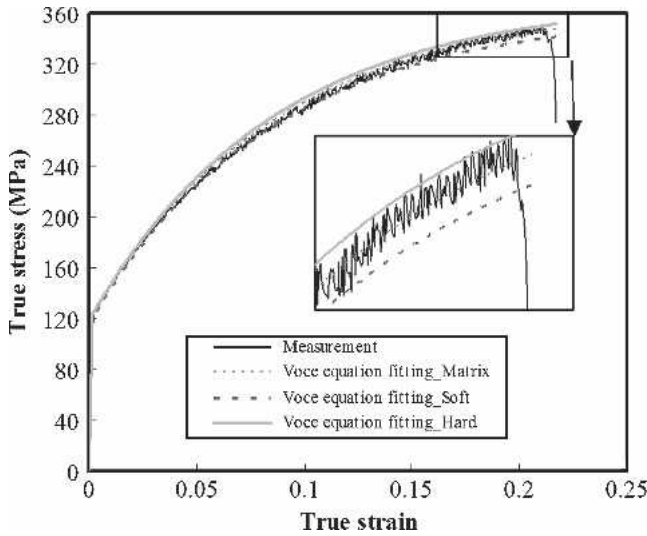METALLURGICAL AND MATERIALS TRANSACTIONS A

Fig. 7—The true stress–true strain curves for various phases (soft, hard, and matrix).
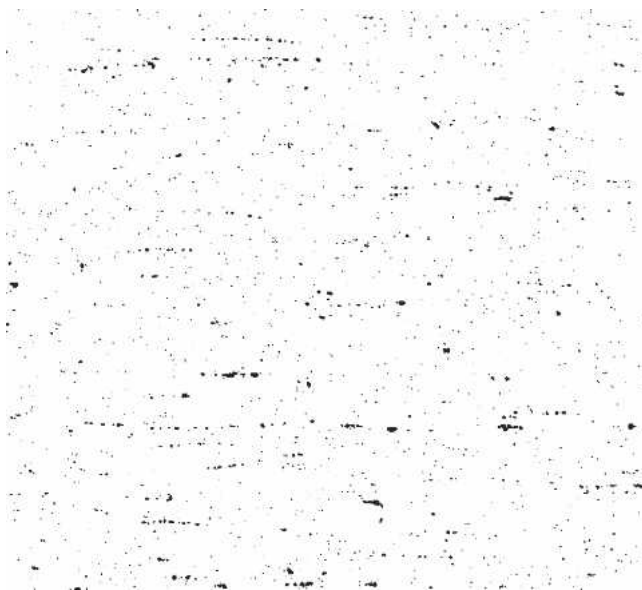

Fig. 8—Particle distribution of an Al-Mg alloy.

size on the response will be discussed in Section VII. The aforementioned method for the determination of stress-strain curves for each phase is obviously different from that shown in Figure 7 and has a clearer physical meaning than the phenomenological method. However, both can be used to predict FLDs.

V. PREDICTED FLD

As stated in Section II, two kinds of finite element models are usually applied in the FLD predictions. In the first part of this section, the results from the use of in-plane plane stress model are described. The FE simulations pertaining to the Nakajima test are reported in the second part.

Because the experimentally measured FLD typically uses a fractured specimen, prediction of the fracture path is necessary in order to have a consistent comparison. The Oyane fracture criterion[16] was used to indicate the initiation of fracture. A physical separation of the specimen was not necessary in the simulation because only the points outside of the intense band were considered in the FLD prediction. The strain values of these points change little during the final fracture process.

The Oyane fracture criterion can be expressed as

$$\int_0^{\bar{\varepsilon}_f} \left(\frac{\sigma_m}{\bar{\sigma}} + B \right) d\bar{\varepsilon} = C \qquad [1]$$

where $\bar{\varepsilon}_f$ is the equivalent strain at fracture initiation, while σ_m and $\bar{\sigma}$ are the hydrostatic stress and the equivalent stress, respectively. The terms B and C are constants. The value of $C = 0.8$ is used in all simulation because it has been justified for a similar Al sheet alloy in Reference 17.

A. In-Plane Plane Stress Model

A plot of equivalent plastic strain rate, as shown in Figures 11 and 12, is most useful for discerning the intense shear band, because outside this region, elastic unloading takes over and there is no further plastic deformation. This kind of plot therefore is used to determine the boundary of the intense shear band and hence the location of the measurement point.

The intense shear bands predicted under uniaxial tension for various specimen geometries are shown in Figure 11. As the notch radius R decreases, a plane strain state is approached in the notched region. The angle between the intense shear band and the applied loading direction also increases from approximately 60 deg (standard uniaxial specimen without a notch[9]) toward 90 deg under plane strain with respect to the loading direction. This agrees well with the experimental observations presented in Figure 1.

For the specimen subjected to biaxial loading, because the same FE model is used in terms of the mesh and the distribution of inhomogeneities for all loading paths, it would be expected that the localization starts from the same place. However, this is only true for the loading ratio $r <$ 0.7 (Figure 12, for instance). As the loading condition approaches the balanced biaxial state, the place of localization shifts. Also noticeable from Figure 12 is that the length of localized band decreases when the critical fracture parameter is reached. Because the damage develops dramatically after the formation of intense shear band, the loading path exerts a significant influence on the characteristics of the fracture pattern.

As mentioned in Section I, the objective of the present article is to develop a methodology for the prediction of FLDs that closely follows the experimental procedure. As the first step, research was carried out to validate our prediction of intense shear bands, in particular, the strain distribution inside and outside of the shear band. The results presented in Figures 11 and 12 are calculated using the stress-strain curves, as shown in Figure 7. Following the same procedure (random distribution of inhomogeneities and the Voce expression of stress-strain curves), the equivalent strain distribution in a flat AA6111-T4 specimen is
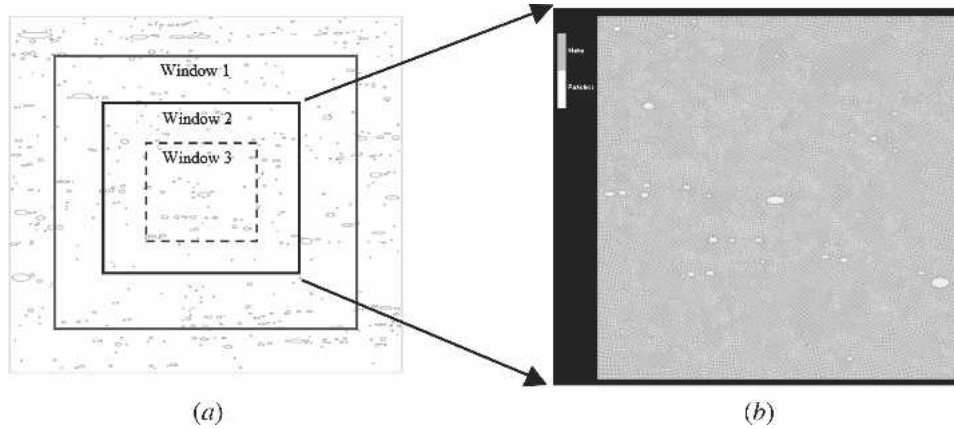
Fig. 9—Micromechanical finite element model. Three concentric windows are selected. Each window consists of two phases: matrix and particles. The particles only undertake elastic deformation. The flow stress behavior of the matrix is taken directly from the uniaxial tension test, as shown in Fig. 7.
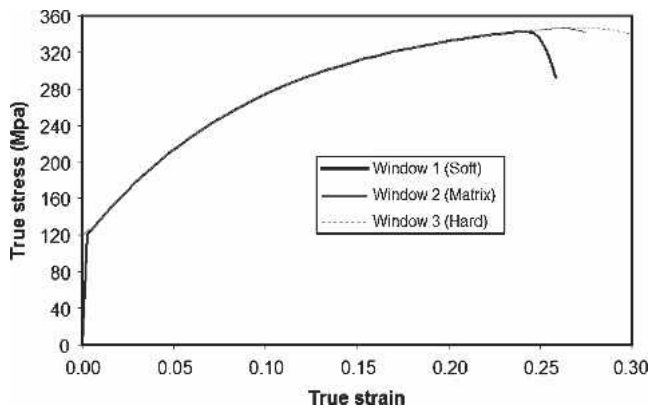

Fig. 10—Calculated true stress–true strain responses from the micromechanical finite element simulations. The three curves represent the responses of the three different windows, as shown in Fig. 9(a). The stress-strain curve that drops earlier is assigned to the soft phase. The stress-strain curve that drops later is assigned to the hard phase. The remaining one is assigned to the matrix.

numerically calculated and compared with the measured values in Figure 13. A noncontact automatic optical strain measurement system was used to experimentally obtain the surface strain evolution leading to Figure 13(b).[18] Clearly, the predicted shear localization agrees well with the strain measurement based on the digital image correlation technique. The reader is referred to Reference 17 for a detailed comparison between the FE prediction and experimental measurements. It should be noted that the predicted intense bandwidth and the orientation to the loading direction depend very little on the spatial distribution of inhomogeneities as long as the inhomogeneities are randomly distributed in the FE structural model. A detailed study of the spatial distribution of inhomogeneities on the localization mode was reported in Reference 9.

Figure 14 shows the distribution of major strain after failure and the minor-major strain profiles for three nodes: one within and two outside the intense shear band. It should be noted that Figures 11(a) and 14(a) are obtained from the same simulation but with different contour plots. The selection of nodes 1 and 2 is made using a plot of equivalent plastic strain rate in Figure 11 based on the criterion of

being the closest node to the shear band and possessing zero plastic strain rate. It is clear from Figure 14(b) that the strain values approach saturation for nodes 1 and 2 after the formation of intense shear band but that node 3 still experiences an increasing minor strain. The small window in Figure 14(b) showing the expanded region of the graph also suggests that node 1 is closer to a plane strain state as the slope of the curve approaches vertical in strain space. Figure 14(c) plots the histories of minor and major strain as a function the increment number. Clearly, both the major and minor strain components saturate after a critical strain is reached (in this case about increment number 45), indicating the formation of an intense shear band. Based on the preceding analysis, nodes 1 and 2 were selected as locations corresponding to the forming limit strains. It should be noted that there are many other points that are also qualified as in the experimental measurement procedure. These points can be easily selected and confirmed by their plot of minor-major strains. Of particular interest are those points that are very close to the corner of two intersecting fracture paths (as shown in Figure 12 for $r = 0.1$). The calculated minor limit strain at these locations is usually greater than anywhere else because of the strain path change.

Following the previously mentioned procedure of using the phenomenological stress-strain curves, we can obtain the forming limit strains for different specimens undergoing other strain paths. The final prediction is shown in Figure 15, identified as "Prediction 1." The modeling-based data points are shown in the filled diamond in Figure 15(a) and the black solid line in Figure 15(b). The solid curves are the trend lines of the predicted discrete data. The crosses are the measurements from seven independent research laboratories.[10] Clearly, a remarkable agreement has been obtained. The measured data points in Figure 15 indicate a significant scatter in the data especially for the plane strain and balanced biaxial strain states. The same is true for the FE predictions.

Selecting the element in the vicinity of a shear band was repeated for analyses with the microstructurally based stress-strain curves obtained from micromacro modeling (Figure 10). The predicted forming limit strains, identified by "Prediction 2," are shown in the filled triangular symbols in Figure 15(a) and the corresponding trend line in Figure 15(b).
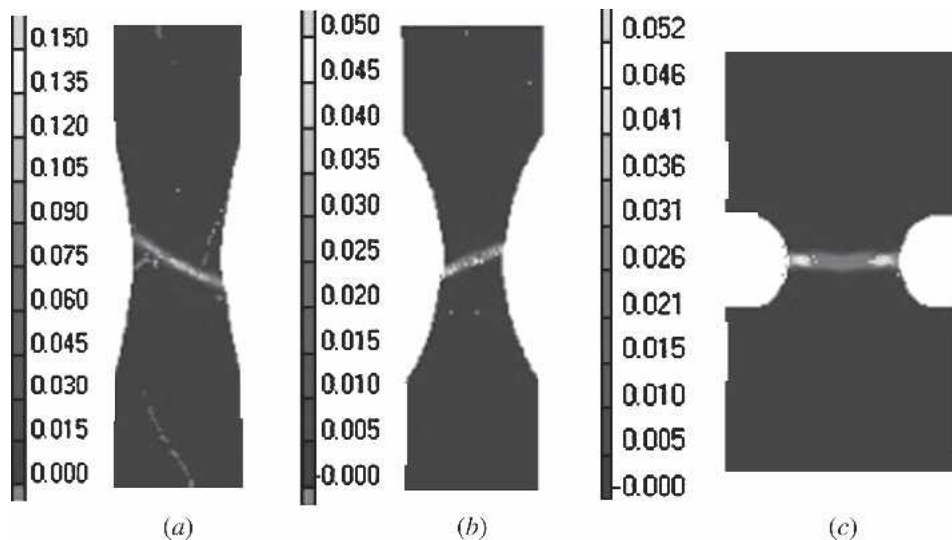
Fig. 11—Predicted shear localization pattern for various specimens under uniaxial tension.
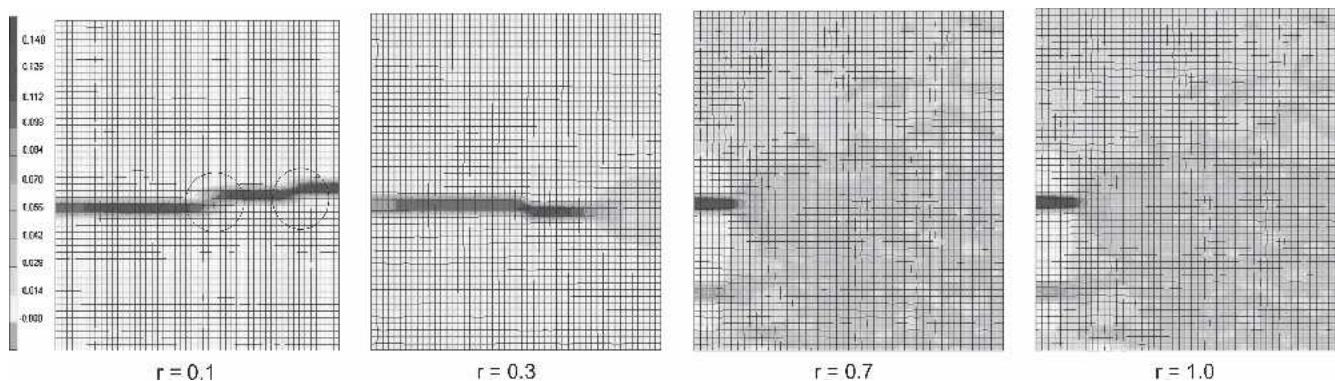

Fig. 12—Predicted shear localization pattern under various strain paths under biaxial loading.

B. 3-D Model for Nakajima Test

The sequence of deformation under uniaxial tension for both sheet Al alloys and steels consists of uniform deformation, diffuse necking, the formation of a crossed band similar to that shown in Figure 1(c), localized necking, and finally void formation and growth in the shear band leading to final failure.[19] Because the preceding deformation sequence is observed in uniaxial tension, the deformation zone is not affected by either the external tooling contact or interfacial friction.

Figure 16 presents the sequence of deformation of a narrow specimen (24 mm in width) stretched by a hemispherical dome. The plotted contour is the equivalent plastic strain rate over the sample surface. Comparable with our previous observations in Reference 19, there is no uniform deformation zone in the center region of the blank because of the existence of contact exerted by the tooling and friction. The ring shape strain rate contour in Figure 16(b) reflects the instantaneous contact boundary between the punch and the blank. Another noticeable feature is the rotation of the intense shear band in the later deformation stage to conform to the punch profile. These features of the

Nakajima test process suggest important differences between the in-plane frictionless deformation mode and the out-of-plane deformation mode of the sheet with punch. It is likely that the limit strain predictions from the two simulation methods will be different.

As stated earlier, different strain paths on the right side of FLD were obtained numerically by changing the lubrication conditions in the Nakajima test. Figure 17 indicates the predicted failure modes under the two friction conditions. It can be clearly seen that the location of the localized bands moves up as the friction coefficient decreases. This is in good agreement with experimental observations in Figure 18.

The predicted FLDs from these 3-D simulations are identified by "Prediction 3," shown as the filled square in Figure 15(a), and the corresponding trend line in Figure 15(b). Again, a reasonable prediction is given.

VI. SENSITIVITY STUDY OF INHOMOGENEITY

A sensitivity study was also carried out to assess the effect of the volume fraction of heterogeneities and their
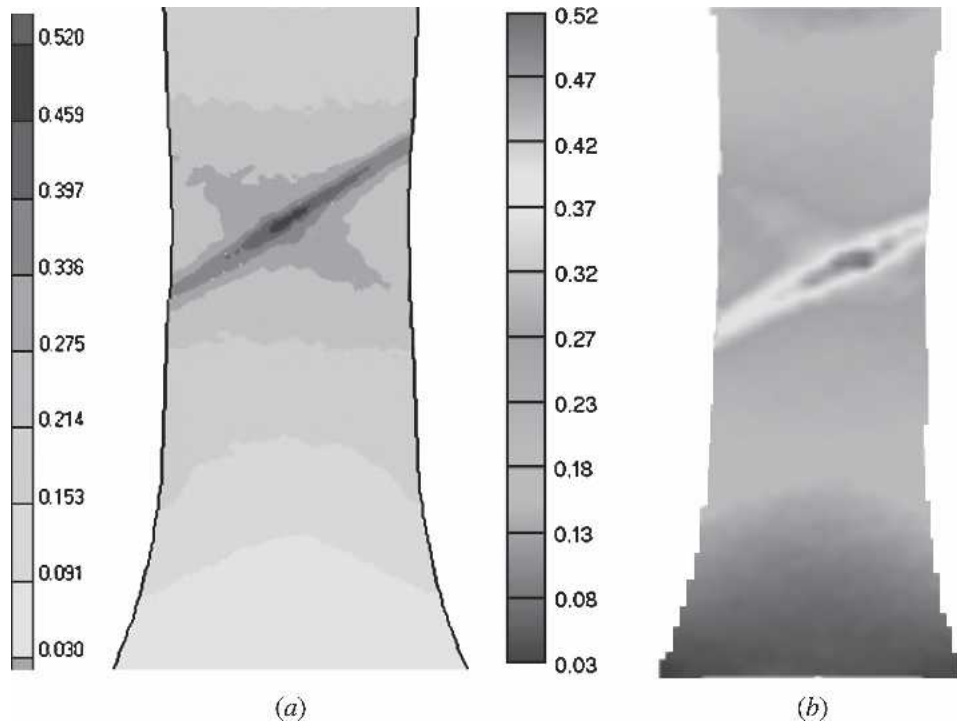
Fig. 13—Comparison between the (*a*) FE predicted and (*b*) measured strain distribution for AA6111-T4.

local strength variation on the predicted limit strains, by the Taguchi method. The Taguchi method adopts a set of standard orthogonal arrays (OAs) to determine the configuration of parameters and analyze the results. The arrays use a small number of experimental runs to obtain maximum information with high reproducibility and reliability.

Four general adjustable parameters were used in the present heterogeneous model: the local strength difference between the soft (or hard) phase and the matrix (Dys_soft and Dys_hard) and the volume fraction of each phase (Vol_soft and Vol_hard). A random distribution of each phase was assumed in the analysis. Each of the parameters was assigned three values (also called "levels"). These values are shown in Table I. The value of Vol_soft and Vol_hard ranged from 10 to 30 pct. The strength increments ranged from 1 to 4 pct. Thus, the flow strength of the soft region is given by $\bar{\sigma}_{\text{soft}} = (1+\text{Dys\_soft})\bar{\sigma}_{\text{matrix}}$ where $\bar{\sigma}_{\text{matrix}}$ is the matrix strength. Similarly, $\bar{\sigma}_{\text{hard}} = (1+\text{Dys\_hard})\bar{\sigma}_{\text{matrix}}$ for the hard region. The designed orthogonal array, L9(3^4), is shown in Table II. Designation L9(3^4) indicates that there are four parameters; each parameter has three levels and a total of nine test runs need to be conducted. For example, if we consider test 6, the volume fraction of the soft phase is 20 pct, the volume fraction of the hard phase is 30 pct, and the remaining 50 pct is the matrix material. The flow stresses for the soft and hard phases are expressed as $\bar{\sigma}_{\text{soft}} = 0.99\bar{\sigma}_{\text{matrix}}$ and $\bar{\sigma}_{\text{hard}} = 1.02\bar{\sigma}_{\text{matrix}}$. To ensure that all nine test runs have the same overall strength of $\bar{\sigma}_{\text{matrix}}$, a mixture rule is applied to modify the strength of the matrix to adapt to the variations of volume fractions of inhomogeneities. For instance, for test 6, a coefficient k is applied to adjust the flow strength of the matrix to satisfy the following constraint:

$$0.2 * 0.99\bar{\sigma}_{\text{matrix}} + 0.3 * 1.02\bar{\sigma}_{\text{matrix}} + (1 - 0.2 - 0.3)$$
$$* k\bar{\sigma}_{\text{matrix}} = \bar{\sigma}_{\text{matrix}}$$

The corresponding k value is 0.992.

The relative contribution of each parameter toward the major forming limit strain (ε_1) is analyzed *via* the analysis of variance (ANOVA) method. ANOVA uses the sum of squares to quantitatively examine the deviation of the responses of each control factor from the overall experimental mean response.[12] The reader is referred to textbooks such as that in Reference 12 for details. The calculated contributions of each parameter to the major forming limit for the case of biaxial loading with an $r = 0.3$ are shown in the last column of Table III in the form of minor strain and major strain. It can be seen that the relative difference in flow strength between the soft phase and the matrix (Dys_soft) is the most important parameter controlling the major limit strain, followed by the volume fraction of the soft phase, the relative difference in flow strength between the hard phase, and the matrix and the volume fraction of the hard phase. The Dys_soft contributes 70.1 pct to the ε_1, about 3.5 times the contribution of the Vol_hard. The influences of the Dys_hard on the ε_1 are negligible. The average effect of each parameter level on the ε_1 is shown in Figure 19. From Figure 18, it can be seen that ε_1 decreases with linear increasing of Dys_soft. However, there is a clear steady stage for the other three influencing parameters.

VII. DISCUSSION

A micromacro model has been proposed to predict the macroscopic response (the FLD in this article) of materials
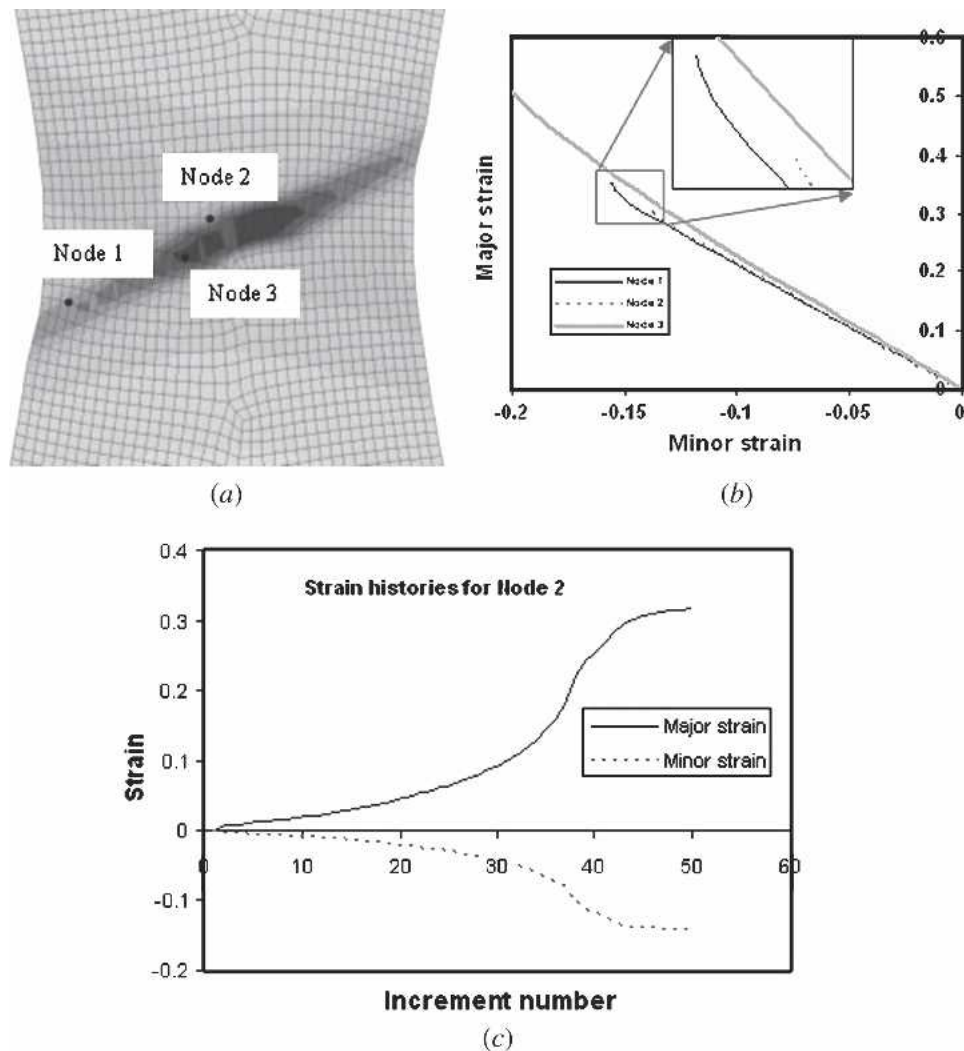
Fig. 14—Minor-major strain profiles for the nodes inside and outside the intense shear bands.

based on microstructural details. Although all three predictions fit well with the measurements in Figure 15, there are still some differences that are worth noting. The best correlation with the data comes from the use of Prediction 1, which is computationally most efficient (Figure 15). Because Prediction 1 and Prediction 2 use exactly the same inhomogeneity distribution and element, the only difference comes from the phenomenological stress-strain curves and the microstructurally based stress-strain curves. As also mentioned from the studies using the Taguchi methods, it is the strength difference between the soft phase and the matrix that dominates the forming limit strain. If we compare the curves in Figure 7 to those in Figure 10, we can see that the strength difference between soft/hard phases to the matrix is larger in Figure 7 than those in Figure 10. In other words, the strength differences in the microstructurally based stress-strain curves from the micromechanical analysis do not ''truly'' reflect the extent of inhomogeneities. This is understandable because only the real particle information is considered and the volume fraction of particles is less than 3 pct. Other important microstructural information such as the texture should be taken into account. This will

certainly add considerable technical difficulty in terms of coupling the particles with texture. The advantage of the model Prediction 1 is even obvious when the FEM is used to predict the forming process of a large automotive part such as a door panel. Although the methodology has been proposed based on MSC.MARC, it can be easily transferred to other commercial programs such as LS-DYNA and ABAQUS.

The relationship between the window size in Figure 9 and the responses in Figure 10 needs to be further interpreted. Although the same unit cell concept is applied, our use of unit cells is rather different compared with work reported in the literature,[4,5] in which the unit cell approach is used to determine a ''representative'' volume element (RVE). The objective in the latter case is to model the behavior of the entire specimen through the analysis of a small but representative volume. Thus, the RVE should be large enough that the results are more or less independent of element size. The purpose of the present microscale modeling approach however is to create a model that captures the inhomogeneity that is inherent in any microstructure and to study how this can be used to trigger
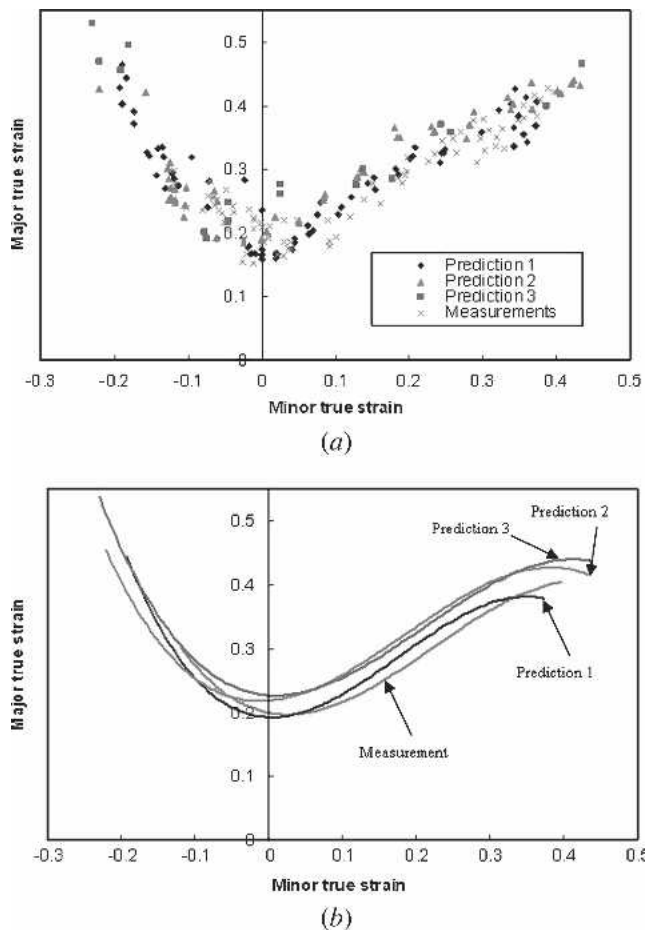
Fig. 15—Comparison between the predicted and measured FLD[9] for AA5182-O. Prediction 1 is obtained by the use of an in-plane plane stress model with the phenomenological stress-strain curves (Fig. 7). Prediction 2 is obtained by use of the in-plane plane stress model with microstructurally based stress-strain curves (Fig. 10). Prediction 3 is obtained by the use of a 3-D model with microstructurally based stress-strain curves (Fig. 10).

localization in the structural scale modeling. It is therefore important that the window be small enough that it captures local features and is therefore not representative of the overall behavior; in other words, it must not be an RVE. Nevertheless, the window size in the current study should not be too small to avoid any substantial changes in terms of the volume fraction of particles. The minimum window size of 40×40 μm was applied in Figure 9. The average particle size is 1 μm.

We also conducted the search of RVE for several Al alloys with different particle volume fractions. Our detailed numerical analyses, not shown in this article, indicated that as the window size increases, localization occurs earlier, resulting in an early drop of the load response. This is also reflected in the results shown in Figure 10. The area fraction of particles varies from 1.68, 1.08, to 1.69 pct as the window's size increases from 40×40 μm, 80×80 μm, to 120×120 μm in Figure 9. The initiation of localization was found to be very sensitive to the largest particle clusters in the unit cell and less sensitive to the most cited volume fraction of microstructure (particles). As the window size increases, the proba-

bility of capturing such a big defect also increases. This is in contrast to most previous work, which only considers the volume fraction of microstructure (particles/textural components) in their microscale[4] or mesoscale[5] models. Under such a circumstance, a representative volume element is rather difficult to establish. To overcome these shortcomings, the selected particle field was encapsulated with a particle free frame that has a slightly larger yield stress. More information on this topic will be reported elsewhere. We refer to other publications[20,21,22] for the determination of minimum RVE size.

Prediction 3 (3-D shell element model with microstructurally based stress-strain curves) tends to overpredict the FLD especially on the right side. The deviation with the measurement in the left side of FLD is significantly less than that on the right side of FLD. This might relate to the element formulation (for instance, solid *vs* shell), different friction models, and the microstructurally based stress-strain curves. More work needs to be conducted in the future to identify why the 3-D model overpredicts the FLD.

Most commercially rolled Al sheet materials exhibit some anisotropy. Their yielding behavior is not well represented by von Mises type of isotropic yield function. More advanced yield functions such as those proposed by Barlat[23,24] should be investigated. However, the aforementioned measured strain distribution from ARAMIS and the FLDs from seven independent laboratories have both demonstrated the applicability of von Mises yield function for the prediction of FLD for Al-Mg sheet alloys using the present heterogeneous microstructurally based finite element model. An advantage of using von Mises yield function is that the analysis time can be significantly reduced.

As mentioned earlier, the present methodology follows from that used to determine FLDs experimentally, enabling a direct comparison with the experimental data. Therefore, our FE models are tuned to mimic experimentally used specimens. However, it is not necessary to use physical specimens such as those in Figure 3. The left side of the FLD can also be calculated from the model in Figure 4 by varying the displacement ratio from -0.5 (uniaxial tension) through zero (in-plane plane strain tension) to 1 (equibiaxial tension). Although the predicted FLDs from both methods show no difference, a model such as that in Figure 4 would make the predicted left- and right-hand sides more consistent.

Unlike all the approaches reported in the literature, the present FE model has the following features.(1) The location and the size of the intense shear band are unknown before analysis. This is contrary to the assumption adopted in the well-known Marciniak–Kuczynski (M-K approach)[25] by which the predicted FLD is very sensitive to the size and orientation of the assumed defect. Also, a measured forming limit strain usually at the in-plane strain state is required to adjust the imperfection factor in the M-K method. This has been an important weakness of the M-K method. (2) Shear localization is not triggered by damage. This is different from those numerical models based on damage evolution, using the GTN[26,27] model, for example. Our recent experimental observation on automotive aluminum alloys indicates that it is the intense deformation that
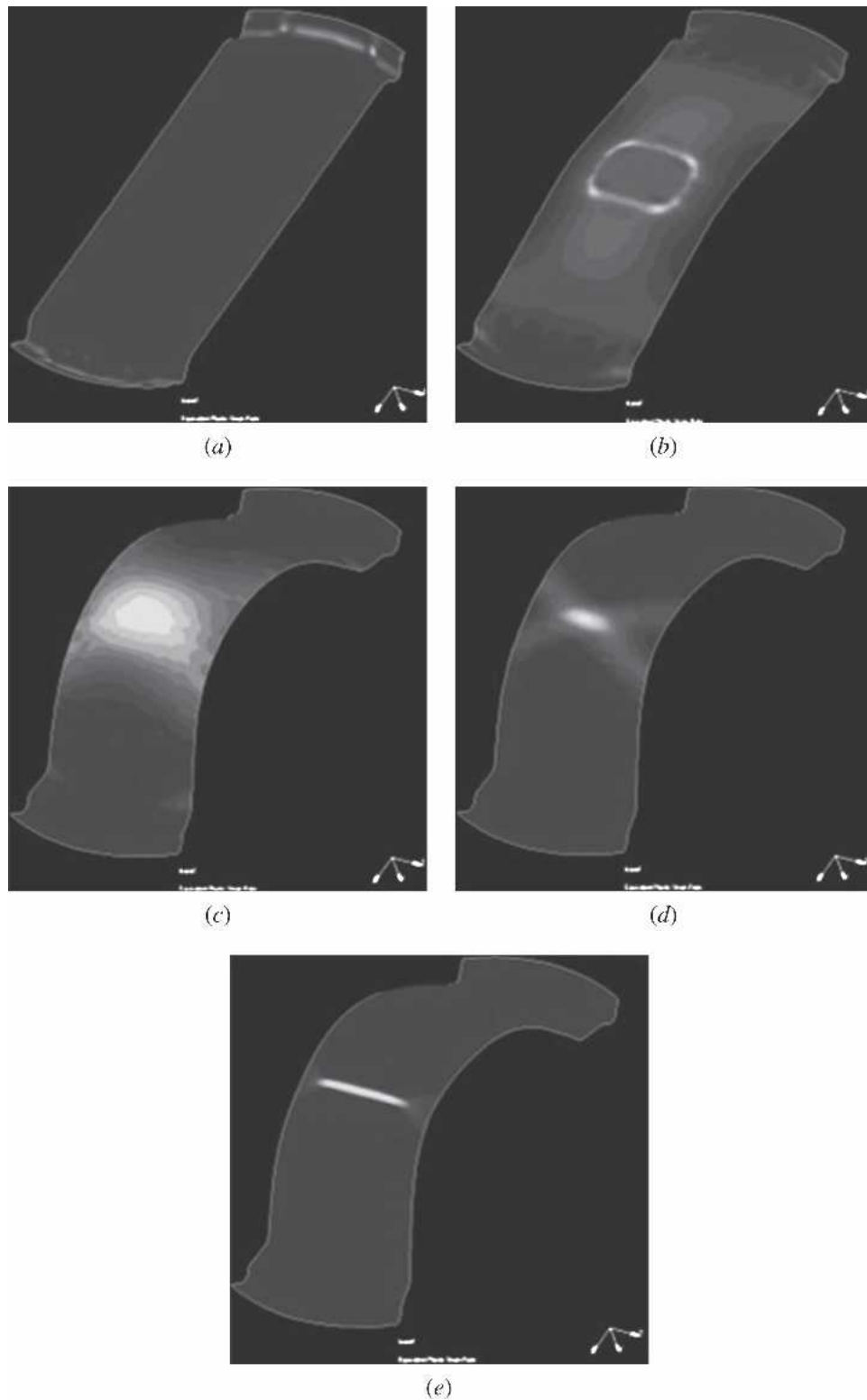
Fig. 16—Sequence of deformation under Nakajima test. The plotted contour is the equivalent plastic strain rate: (*a*) end of clamping, (*b*) the ring represents the instantaneous contact condition between the punch and blank, (*c*) diffuse necking, (*d*) crossed bands, and (*e*) localized necking and failure.

accompanies localization that promotes damage nucleation and growth.[19] (3) The fracture criterion is introduced as a user-defined postprocessing variable in the FE computation to select the measurement point. The implementation of a

fracture criterion does not affect the calculated strain values. Once the critical fracture parameter is exceeded, we assume that the fracture path and pattern have been completely established. The actual fracture need not be simulated.
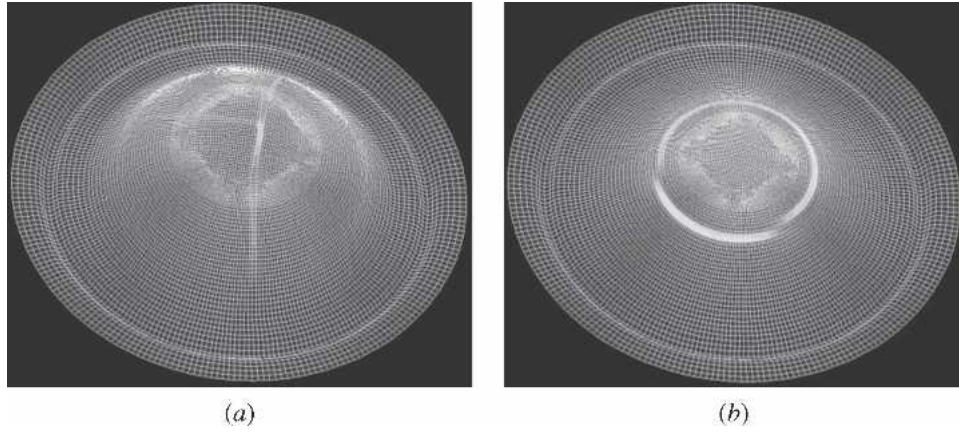
Fig. 17—Failure modes under different friction conditions: (*a*) no friction and (*b*) friction coefficient of 0.1.
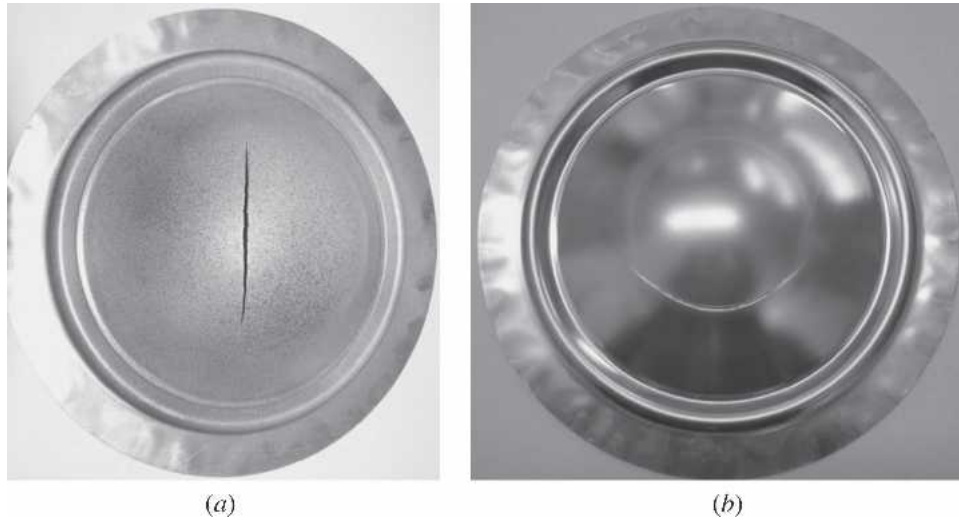

Fig. 18—Experimentally observed failure modes under different friction conditions: (*a*) Teflon and (*b*) dry condition.

Table I.   Test Parameters and Their Levels

Variable	Level 1	Level 2	Level 3
Vol_soft	10 pct	20 pct	30 pct
Vol_hard	10 pct	20 pct	30 pct
Dys._soft	−1 pct	−2 pct	−4 pct
Dys._hard	1 pct	2 pct	4 pct

(4) The model has the flexibility to take into account the microstructural information at different length scales.

VIII. CONCLUSIONS

A new methodology has been developed to predict the FLD and has been applied to Al-Mg alloys. The new methodology follows from that used to determine FLDs experimentally, enabling a direct comparison with the experimental data. The predicted FLD for AA5182-O fits remarkably well with the measurements from a recent round robin experimental FLD program involving several research laboratories. The influence of the parameters

Table II.   Experimental Design

Test	Vol_soft	Vol_hard	Dys_soft	Dys._hard	Forming Limit Strain
1	10 pct	10 pct	−1 pct	1 pct	0.077, 0.236
2	10 pct	20 pct	−2 pct	2 pct	0.068, 0.204
3	10 pct	30 pct	−4 pct	4 pct	0.053, 0.178
4	20 pct	10 pct	−2 pct	4 pct	0.074, 0.219
5	20 pct	20 pct	−4 pct	1 pct	0.058, 0.18
6	20 pct	30 pct	−1 pct	2 pct	0.068, 0.209
7	30 pct	10 pct	−4 pct	2 pct	0.056, 0.182
8	30 pct	20 pct	−1 pct	4 pct	0.066, 0.199
9	30 pct	30 pct	−2 pct	1 pct	0.071, 0.197

Table III.   Analysis of Variance

	Vol_soft	Vol_hard	Dys_soft	Dys_hard
SS pct	8.6 pct	19.5 pct	70.1 pct	1.8 pct

describing the inhomogeneity is also studied by the Taguchi method. It has been found that the calculated major forming limit strain is very sensitive to the assumed relative difference in the flow strength between the soft phase and the
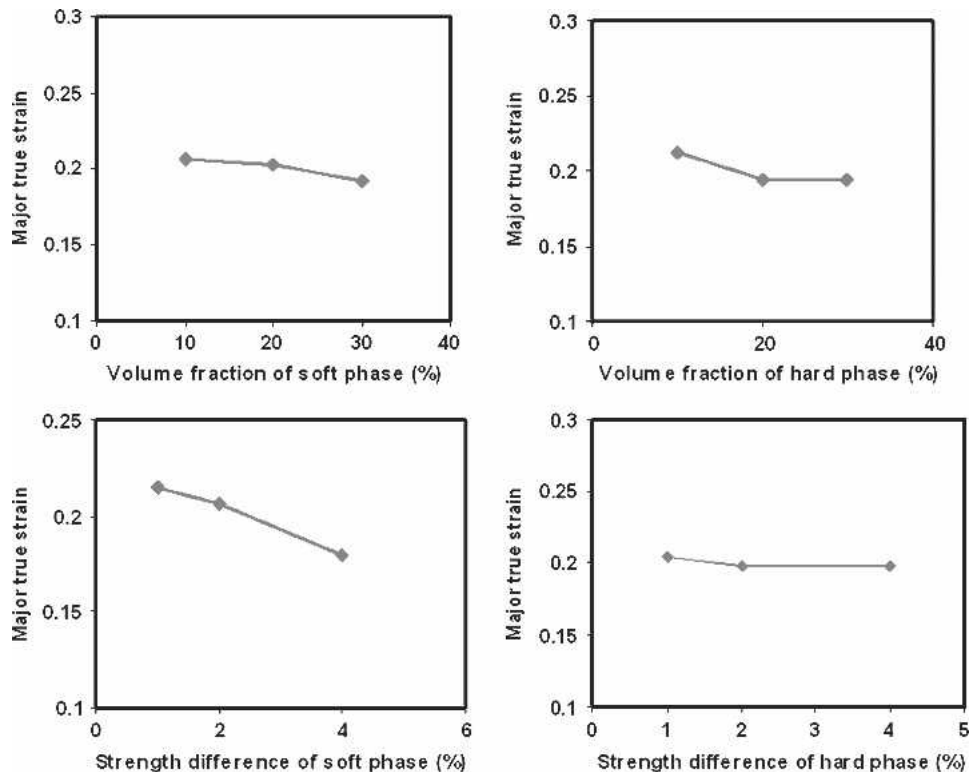
Fig. 19—Plots of response of each parameter level on the predicted ε_1 for the subsurface point.

matrix. The influence of its volume fraction is minor. The predicted FLD based on modeling the 3-D dome test tends to overpredict the right side of FLD. As long as meaningful microstructural parameters are assigned to the inhomogeneities, the use of phenomenological stress-strain curves with the in-plane plane stress model is recommended because it is the most accurate and efficient approach.

ACKNOWLEDGMENTS

REFERENCES

1. K. Narasimhan and R.H. Wagoner: *Metall. Trans. A*, 1991, vol. 22, pp. 2655-65.
2. M. Jain, D.J. Lloyd, and S.R. MacEwen: *Int. J. Mech. Sci.*, 1996, vol. 38, pp. 219-32.
3. P.D. Wu, K.W. Neale, and E. Van der Giessen: *Proc. R. Soc. London, Ser. A: Math., Phys. Eng. Sci.*, 1997, vol. 453, pp. 1831-48.
4. H.P. Gänser, E.A. Werner, and F.D. Fischer: *Int. J. Mech. Sci.*, 2000, vol. 42, pp. 2041-54.
5. P.D. Wu, S.R. MacEwen, D.J. Lloyd, and K.W. Neale: *Modell. Simul. Mater. Sci. Eng.*, 2004, vol. 12, pp. 511-27.
6. K. Inal, K.W. Neale, and A. Aoutajeddine: *Int. J. Plast.*, 2005, vol. 21, pp. 1255-66.
7. K. Janssens, F. Lambert, S. Vanrostenberghe, and M. Vermeulen: *J. Mater. Process. Technol.*, 2001, vol. 112, pp. 174-84.
8. R. Hill: *J. Mech. Phys. Solids*, 1952, vol. 1, pp. 19-30.
9. X. Duan, M. Jain, D. Metzger, J. Kang, D.S. Wilkinson, and J.D. Embury: *Mater. Sci. Eng., A*, 2005, vol. 394, pp. 192-203.
10. W. Hotz: *GOM User Meeting*, Braunschweig, Germany, 2004.
11. K. Nakajima, T. Kikuuma, and K. Hasuka: "Yawata Technical Report No. 284," Yawata, Japan, 1971, pp. 678-90.
12. W.Y. Fowlkes and C.M. Creveling: *Engineering Methods for Robust Product Design Using Taguchi Methods in Technology and Product Development*, Addison-Wesley, Reading, MA, 1995.
13. D.R. Metzger, X. Duan, and M. Jain: Paper presented at the American Society of Mechanical Engineers, Pressure Vessels and Piping Division, Denver, CO, July 17–21, 2005, Paper Number PVP2005-71383.
14. M. Moore and P. Bate: *J. Mater. Process. Technol.*, 2002, vols. 125–26, pp. 258-66.
15. E. Voce: *J. Inst. Met.*, 1948, vol. 74, pp. 537-62.
16. M. Oyane, T. Sato, K. Okimoto, and S. Shima: *J. Mech. Working Technol.*, 1980, vol. 4, pp. 65-81.
17. X. Duan, M. Bruhis, M. Jain, and D.S. Wilkinson: *Adv. Mater. Res.*, 2005, vol. 66, pp. 737-44.
18. *ARAMIS 4.7*, GOM mbH, Braunschweig, Germany, 2001.
19. X. Duan, Y. Osokov, M. Jain, D.R. Metzger, and D.S. Wilkinson: unpublished report, McMaster University, Hamilton, Canada, 2005.
20. C. Liu: *Exp. Mech.*, 2005, vol. 45, pp. 238-43.
21. Z.Y. Ren and Q.S. Zheng: *J. Mech. Phys. Solids*, 2002, vol. 50, pp. 881-93.
22. P.D. Wu and D.J. Lloyd: *Acta Mater.*, 2004, vol. 52, pp. 1785-98.
23. F. Barlat, D.J. Ledge, and J.C. Brem: *Int. J. Plast.*, 1991, vol. 7, pp. 693-712.
24. F. Barlat, J.C. Brem, J.W. Yoon, K. Chung, R.E. Dick, D.J. Lege, F. Pourboghrat, S.H. Choi, and E. Chu: *Int. J. Plast.*, 2003, vol. 19, pp. 1297-319.
25. Z. Marciniak and K. Kuczynski: *Int. J. Mech. Sci.*, 1967, vol. 9, pp. 609-20.
26. A.L. Gurson: *J. Eng. Mater. Technol.*, 1977, vol. 99, pp. 2-15.
27. V. Tvergaard and A. Needleman: *Acta Metall.*, 1984, vol. 32, pp. 461-90.